Research Article | Vol. 8, No. 1 | 1 Jan 2017 | BIOMEDICAL OPTICS EXPRESS 16

Biomedical Optics EXPRESS

Wide-field retinal optical coherence tomography with wavefront sensorless adaptive optics for enhanced imaging of targeted regions

JAMES POLANS,[1,*] BRENTON KELLER,[1] OSCAR M. CARRASCO-ZEVALLOS,[1] FRANCESCO LAROCCA,[1] ELIJAH COLE,[1] HEATHER E. WHITSON,[2,3,4] ELEONORA M. LAD,[2] SINA FARSIU,[1,2] AND JOSEPH A. IZATT[1,2]

[1]*Department of Biomedical Engineering, Duke University, 136 Hudson Hall, Box 90281, Durham, North Carolina 27708, USA*
[2]*Department of Ophthalmology, Duke University Medical Center, Durham, North Carolina 27710, USA*
[3]*Department of Medicine (Geriatrics)/Duke Aging Center, Duke University Medical Center, Durham, North Carolina 27710, USA*
[4]*Geriatrics Research Education & Clinical Center, Durham VA Medical Center, Durham, North Carolina 27705, USA*
[*]*jpolans@duke.edu*

Abstract: The peripheral retina of the human eye offers a unique opportunity for assessment and monitoring of ocular diseases. We have developed a novel wide-field (>70°) optical coherence tomography system (WF-OCT) equipped with wavefront sensorless adaptive optics (WSAO) for enhancing the visualization of smaller (<25°) targeted regions in the peripheral retina. We iterated the WSAO algorithm at the speed of individual OCT B-scans (~20 ms) by using raw spectral interferograms to calculate the optimization metric. Our WSAO approach with a 3 mm beam diameter permitted primarily low- but also high- order peripheral wavefront correction in less than 10 seconds. In preliminary imaging studies in five normal human subjects, we quantified statistically significant changes with WSAO correction, corresponding to a 10.4% improvement in average pixel brightness (signal) and 7.0% improvement in high frequency content (resolution) when visualizing 1 mm (~3.5°) B-scans of the peripheral (>23°) retina. We demonstrated the ability of our WF-OCT system to acquire non wavefront-corrected wide-field images rapidly, which could then be used to locate regions of interest, zoom into targeted features, and visualize the same region at different time points. A pilot clinical study was conducted on seven healthy volunteers and two subjects with prodromal Alzheimer's disease which illustrated the capability to image Drusen-like pathologies as far as 32.5° from the fovea in un-averaged volume scans. This work suggests that the proposed combination of WF-OCT and WSAO may find applications in the diagnosis and treatment of ocular, and potentially neurodegenerative, diseases of the peripheral retina, including diabetes and Alzheimer's disease.

OCIS codes: (330.4060) Vision modeling, (330.7326) Visual optics, modeling; (330.4460) Ophthalmic optics and devices, (330.7327) Visual optics, ophthalmic instrumentation, (170.4470) Ophthalmology, (170.4500) Optical coherence tomography.

References and links

1. D. Huang, E. A. Swanson, C. P. Lin, J. S. Schuman, W. G. Stinson, W. Chang, M. R. Hee, T. Flotte, K. Gregory, C. A. Puliafito, and J. G. Fujimoto, "Optical Coherence Tomography," Science **254**(5035), 1178–1181 (1991).
2. A. F. Fercher, C. K. Hitzenberger, W. Drexler, G. Kamp, and H. Sattmann, "In Vivo Optical Coherence Tomography," Am. J. Ophthalmol. **116**(1), 113–114 (1993).
3. J. S. Schuman, C. A. Puliafito, J. G. Fujimoto, and J. S. Duker, *Optical Coherence Tomography of Ocular Diseases,* 3rd ed. (Slack Inc., Thorofare, New Jersey, USA, 2012).
4. O. Pomerantzeff, "Equator-Plus Camera," Invest. Ophthalmol. **14**(5), 401–406 (1975).

#261368 http://dx.doi.org/10.1364/BOE.8.000016
Journal © 2017 Received 7 Apr 2016; revised 28 Oct 2016; accepted 19 Nov 2016; published 2 Dec 2016

Biomedical Optics EXPRESS

5. M. M. Wessel, G. D. Aaker, G. Parlitsis, M. Cho, D. J. D'Amico, and S. Kiss, "Ultra-Wide-Field Angiography Improves the Detection and Classification of Diabetic Retinopathy," Retina **32**(4), 785–791 (2012).
6. L. Reznicek, T. Klein, W. Wieser, M. Kernt, A. Wolf, C. Haritoglou, A. Kampik, R. Huber, and A. S. Neubauer, "Megahertz ultra-wide-field swept-source retina optical coherence tomography compared to current existing imaging devices," Graefes Arch. Clin. Exp. Ophthalmol. **252**(6), 1009–1016 (2014).
7. R. D. Ferguson, Z. Zhong, D. X. Hammer, M. Mujat, A. H. Patel, C. Deng, W. Zou, and S. A. Burns, "Adaptive optics scanning laser ophthalmoscope with integrated wide-field retinal imaging and tracking," J. Opt. Soc. Am. A **27**(11), A265–A277 (2010).
8. R. P. McNabb, D. S. Grewal, R. Mehta, S. G. Schuman, J. A. Izatt, T. H. Mahmoud, G. J. Jaffe, P. Mruthyunjaya, and A. N. Kuo, "Wide field of view swept-source optical coherence tomography for peripheral retinal disease," Br. J. Ophthalmol. **100**(10), 1377–1382 (2016).
9. A. Manivannan, J. Plskova, A. Farrow, S. Mckay, P. F. Sharp, and J. V. Forrester, "Ultra-wide-field fluorescein angiography of the ocular fundus," Am. J. Ophthalmol. **140**(3), 525–527 (2005).
10. V. L. L. Torres, N. Brugnoni, P. K. Kaiser, and A. D. Singh, "Optical Coherence Tomography Enhanced Depth Imaging of Choroidal Tumors," Am. J. Ophthalmol. **151**(4), 586–593 (2011).
11. T. Klein, W. Wieser, C. M. Eigenwillig, B. R. Biedermann, and R. Huber, "Megahertz OCT for ultrawide-field retinal imaging with a 1050 nm Fourier domain mode-locked laser," Opt. Express **19**(4), 3044–3062 (2011).
12. J. P. Kolb, T. Klein, C. L. Kufner, W. Wieser, A. S. Neubauer, and R. Huber, "Ultra-widefield retinal MHz-OCT imaging with up to 100 degrees viewing angle," Biomed. Opt. Express **6**(5), 1534–1552 (2015).
13. J. Polans, B. Jaeken, R. P. McNabb, P. Artal, and J. A. Izatt, "Wide-field optical model of the human eye with asymmetrically tilted and decentered lens that reproduces measured ocular aberrations," Optica **2**, 124–134 (2015).
14. B. Jaeken and P. Artal, "Optical Quality of Emmetropic and Myopic Eyes in the Periphery Measured with High-Angular Resolution," Invest. Ophthalmol. Vis. Sci. **53**(7), 3405–3413 (2012).
15. P. Bedggood, M. Daaboul, R. Ashman, G. Smith, and A. Metha, "Characteristics of the human isoplanatic patch and implications for adaptive optics retinal imaging," J. Biomed. Opt. **13**(2), 024008 (2008).
16. A. V. Dubinin, T. Y. Cherezova, A. I. Belyakov, and A. V. Kudryashov, "Isoplanatism of the optical system of the human eye," J. Opt. Technol. **75**, 172–174 (2008).
17. M. Nowakowski, M. Sheehan, D. Neal, and A. V. Goncharov, "Investigation of the isoplanatic patch and wavefront aberration along the pupillary axis compared to the line of sight in the eye," Biomed. Opt. Express **3**(2), 240–258 (2012).
18. J. Liang, D. R. Williams, and D. T. Miller, "Supernormal vision and high-resolution retinal imaging through adaptive optics," J. Opt. Soc. Am. A **14**(11), 2884–2892 (1997).
19. A. Roorda, F. Romero-Borja, W. Donnelly Iii, H. Queener, T. Hebert, and M. Campbell, "Adaptive optics scanning laser ophthalmoscopy," Opt. Express **10**(9), 405–412 (2002).
20. J. Carroll, M. Neitz, H. Hofer, J. Neitz, and D. R. Williams, "Functional photoreceptor loss revealed with adaptive optics: An alternate cause of color blindness," Proc. Natl. Acad. Sci. U.S.A. **101**(22), 8461–8466 (2004).
21. R. J. Zawadzki, S. M. Jones, S. S. Olivier, M. Zhao, B. A. Bower, J. A. Izatt, S. Choi, S. Laut, and J. S. Werner, "Adaptive-optics optical coherence tomography for high-resolution and high-speed 3D retinal in vivo imaging," Opt. Express **13**(21), 8532–8546 (2005).
22. Y. Zhang, J. Rha, R. Jonnal, and D. Miller, "Adaptive optics parallel spectral domain optical coherence tomography for imaging the living retina," Opt. Express **13**(12), 4792–4811 (2005).
23. B. Hermann, E. J. Fernández, A. Unterhuber, H. Sattmann, A. F. Fercher, W. Drexler, P. M. Prieto, and P. Artal, "Adaptive-optics ultrahigh-resolution optical coherence tomography," Opt. Lett. **29**(18), 2142–2144 (2004).
24. A. Roorda and D. R. Williams, "The arrangement of the three cone classes in the living human eye," Nature **397**(6719), 520–522 (1999).
25. A. Dubra, Y. Sulai, J. L. Norris, R. F. Cooper, A. M. Dubis, D. R. Williams, and J. Carroll, "Noninvasive imaging of the human rod photoreceptor mosaic using a confocal adaptive optics scanning ophthalmoscope," Biomed. Opt. Express **2**(7), 1864–1876 (2011).
26. F. Felberer, J. S. Kroisamer, C. K. Hitzenberger, and M. Pircher, "Lens based adaptive optics scanning laser ophthalmoscope," Opt. Express **20**(16), 17297–17310 (2012).
27. Z. Liu, O. P. Kocaoglu, and D. T. Miller, "In-the-plane design of an off-axis ophthalmic adaptive optics system using toroidal mirrors," Biomed. Opt. Express **4**(12), 3007–3029 (2013).
28. D. C. Chen, S. M. Jones, D. A. Silva, and S. S. Olivier, "High-resolution adaptive optics scanning laser ophthalmoscope with dual deformable mirrors," J. Opt. Soc. Am. A **24**(5), 1305–1312 (2007).
29. Y. Jian, J. Xu, M. A. Gradowski, S. Bonora, R. J. Zawadzki, and M. V. Sarunic, "Wavefront sensorless adaptive optics optical coherence tomography for in vivo retinal imaging in mice," Biomed. Opt. Express **5**(2), 547–559 (2014).
30. K. S. K. Wong, Y. Jian, M. Cua, S. Bonora, R. J. Zawadzki, and M. V. Sarunic, "In vivo imaging of human photoreceptor mosaic with wavefront sensorless adaptive optics optical coherence tomography," Biomed. Opt. Express **6**(2), 580–590 (2015).
31. H. Hofer, N. Sredar, H. Queener, C. Li, and J. Porter, "Wavefront sensorless adaptive optics ophthalmoscopy in the human eye," Opt. Express **19**(15), 14160–14171 (2011).

Biomedical Optics EXPRESS

32. S. Bonora and R. J. Zawadzki, "Wavefront sensorless modal deformable mirror correction in adaptive optics: optical coherence tomography," Opt. Lett. **38**(22), 4801–4804 (2013).
33. M. Wojtkowski, V. Srinivasan, T. Ko, J. Fujimoto, A. Kowalczyk, and J. Duker, "Ultrahigh-resolution, high-speed, Fourier domain optical coherence tomography and methods for dispersion compensation," Opt. Express **12**(11), 2404–2422 (2004).
34. O. A. R. Board, "OpenMP Application Program Interface Version 2.5" (2005), retrieved http://www.openmp.org/mp-documents/spec30.pdf.
35. M. A. Vorontsov, "Decoupled stochastic parallel gradient descent optimization for adaptive optics: integrated approach for wave-front sensor information fusion," J. Opt. Soc. Am. A **19**(2), 356–368 (2002).
36. S. Martinez-Conde, S. L. Macknik, and D. H. Hubel, "The role of fixational eye movements in visual perception," Nat. Rev. Neurosci. **5**(3), 229–240 (2004).
37. R. C. Gonzalez and R. E. Woods, *Digital Image Processing (3rd Edition)* (Prentice-Hall, Inc., 2006).
38. S. J. Chiu, X. T. Li, P. Nicholas, C. A. Toth, J. A. Izatt, and S. Farsiu, "Automatic segmentation of seven retinal layers in SDOCT images congruent with expert manual segmentation," Opt. Express **18**(18), 19413–19428 (2010).
39. B. Dubois and M. L. Albert, "Amnestic MCI or prodromal Alzheimer's disease?" Lancet Neurol. **3**(4), 246–248 (2004).
40. F. LaRocca, D. Nankivil, T. DuBose, S. Farsiu, and J. A. Izatt, "Ultra-compact switchable SLO/OCT handheld probe design," Ophthalmic Technologies Xxv **9307**(2015).
41. D. Nankivil, G. Waterman, F. LaRocca, B. Keller, A. N. Kuo, and J. A. Izatt, "Handheld, rapidly switchable, anterior/posterior segment swept source optical coherence tomography probe," Biomed. Opt. Express **6**(11), 4516–4528 (2015).
42. D. L. Fried, "Anisoplanatism in Adaptive Optics," J. Opt. Soc. Am. **72**, 52–61 (1982).
43. A. V. Goncharov, M. Nowakowski, M. T. Sheehan, and C. Dainty, "Reconstruction of the optical system of the human eye with reverse ray-tracing," Opt. Express **16**(3), 1692–1703 (2008).
44. M. Rueckel and W. Denk, "Properties of coherence-gated wavefront sensing," J. Opt. Soc. Am. A **24**(11), 3517–3529 (2007).
45. J. Porter, H. Queener, J. Lin, K. Thorn, and A. A. Awwal, *Adaptive Optics for Vision Science: Principles, Practices, Design and Applications* (John Wiley & Sons, 2006), Vol. 171.
46. L. Lundström and P. Unsbo, "Unwrapping Hartmann-Shack images from highly aberrated eyes using an iterative B-spline based extrapolation method," Optom. Vis. Sci. **81**(5), 383–388 (2004).
47. S. Koh, N. Maeda, T. Kuroda, Y. Hori, H. Watanabe, T. Fujikado, Y. Tano, Y. Hirohara, and T. Mihashi, "Effect of tear film break-up on higher-order aberrations measured with wavefront sensor," Am. J. Ophthalmol. **134**(1), 115–117 (2002).
48. A. Dubra, C. Paterson, and C. Dainty, "Study of the tear topography dynamics using a lateral shearing interferometer," Opt. Express **12**(25), 6278–6288 (2004).
49. Y. Jian, R. J. Zawadzki, and M. V. Sarunic, "Adaptive optics optical coherence tomography for in vivo mouse retinal imaging," J. Biomed. Opt. **18**(5), 56007 (2013).
50. H. R. G. W. Verstraete, S. Wahls, J. Kalkman, and M. Verhaegen, "Model-based sensor-less wavefront aberration correction in optical coherence tomography," Opt. Lett. **40**(24), 5722–5725 (2015).
51. H. Ishikawa, D. M. Stein, G. Wollstein, S. Beaton, J. G. Fujimoto, and J. S. Schuman, "Macular segmentation with optical coherence tomography," Invest. Ophthalmol. Vis. Sci. **46**(6), 2012–2017 (2005).
52. S. Farsiu, S. J. Chiu, R. V. O'Connell, F. A. Folgar, E. Yuan, J. A. Izatt, C. A. Toth, and A.-R. E. D. S. Ancill; Age-Related Eye Disease Study 2 Ancillary Spectral Domain Optical Coherence Tomography Study Group, "Quantitative Classification of Eyes with and without Intermediate Age-Related Macular Degeneration Using Optical Coherence Tomography," Ophthalmology **121**(1), 162–172 (2014).
53. S. G. Schuman, A. F. Koreishi, S. Farsiu, S. H. Jung, J. A. Izatt, and C. A. Toth, "Photoreceptor Layer Thinning over Drusen in Eyes with Age-Related Macular Degeneration Imaged In Vivo with Spectral-Domain Optical Coherence Tomography," Ophthalmology **116**(3), 488–496 (2009).
54. D. C. Hood, C. E. Lin, M. A. Lazow, K. G. Locke, X. Zhang, and D. G. Birch, "Thickness of Receptor and Post-Receptor Retinal Layers in Patients with Retinitis Pigmentosa Measured with Frequency-Domain Optical Coherence Tomography," Invest. Ophthalmol. Vis. Sci. **50**(5), 2328–2336 (2009).
55. M. D. Davis, S. B. Bressler, L. P. Aiello, N. M. Bressler, D. J. Browning, C. J. Flaxel, D. S. Fong, W. J. Foster, A. R. Glassman, M. E. R. Hartnett, C. Kollman, H. K. Li, H. Qin, I. U. Scott, and Diabetic Retinopathy Clinical Research Network Study Group, "Comparison of time-domain OCT and fundus photographic assessments of retinal thickening in eyes with diabetic macular edema," Invest. Ophthalmol. Vis. Sci. **49**(5), 1745–1752 (2008).
56. D. Cabrera Fernández, H. M. Salinas, and C. A. Puliafito, "Automated detection of retinal layer structures on optical coherence tomography images," Opt. Express **13**(25), 10200–10216 (2005).
57. S. Bearelly, F. Y. Chau, A. Koreishi, S. S. Stinnett, J. A. Izatt, and C. A. Toth, "Spectral Domain Optical Coherence Tomography Imaging of Geographic Atrophy Margins," Ophthalmology **116**(9), 1762–1769 (2009).
58. S. J. Chiu, C. A. Toth, C. Bowes Rickman, J. A. Izatt, and S. Farsiu, "Automatic segmentation of closed-contour features in ophthalmic images using graph theory and dynamic programming," Biomed. Opt. Express **3**(5), 1127–1140 (2012).
59. C. Li, N. Sredar, K. M. Ivers, H. Queener, and J. Porter, "A correction algorithm to simultaneously control dual deformable mirrors in a woofer-tweeter adaptive optics system," Opt. Express **18**(16), 16671–16684 (2010).

Biomedical Optics EXPRESS

60. R. K. Wang, S. L. Jacques, Z. Ma, S. Hurst, S. R. Hanson, and A. Gruber, "Three dimensional optical angiography," Opt. Express **15**(7), 4083–4097 (2007).
61. S. Makita, Y. Hong, M. Yamanari, T. Yatagai, and Y. Yasuno, "Optical coherence angiography," Opt. Express **14**(17), 7821–7840 (2006).
62. M. Patel and S. Kiss, "Ultra-wide-field fluorescein angiography in retinal disease," Curr. Opin. Ophthalmol. **25**(3), 213–220 (2014).
63. A. N. Kuo, R. P. McNabb, S. J. Chiu, M. A. El-Dairi, S. Farsiu, C. A. Toth, and J. A. Izatt, "Correction of Ocular Shape in Retinal Optical Coherence Tomography and Effect on Current Clinical Measures," Am. J. Ophthalmol. **156**(2), 304–311 (2013).
64. O. Carrasco-Zevallos, D. Nankivil, B. Keller, C. Viehland, B. J. Lujan, and J. A. Izatt, "Pupil tracking optical coherence tomography for precise control of pupil entry position," Biomed. Opt. Express **6**(9), 3405–3419 (2015).
65. A. H. Dhalla, D. Nankivil, T. Bustamante, A. Kuo, and J. A. Izatt, "Simultaneous swept source optical coherence tomography of the anterior segment and retina using coherence revival," Opt. Lett. **37**(11), 1883–1885 (2012).

1. Introduction

Since its inception, optical coherence tomography (OCT) [1, 2] has achieved widespread adoption in clinical ophthalmology in part due to its ability to visualize retinal tissue in three dimensions. While many applications have focused on the central macula [3], commercial clinical OCT systems have begun to expand their field-of-view (FOV) from 30° to 55°. Two-dimensional *en face* ophthalmic imaging techniques, including fundus [4] and fluorescence imaging [5], can record a wider FOV (sometimes >100°), but they cannot monitor peripheral disease processes in three dimensions.

There has been increasing interest to obtain three-dimensional high-resolution images of peripheral pathologies [6–8]. This growing interest stems from the notion that the peripheral retina offers a unique perspective towards the assessment and monitoring of certain ocular diseases [8], including diabetic retinopathy [5], retinal vein occlusion [9], and choroid masses [10]. Several wide-field OCT (WF-OCT) systems [8, 11, 12] have been developed previously, offering an alternative solution to mosaicking. Current state-of-the-art WF-OCT systems have demonstrated impressive capabilities, with >90 dB sensitivities and FOV up to 100° [12]. However, as discussed in [12], prior systems suffered from a loss of signal and transverse resolution at extreme FOV due to field curvature of the retina, angle-dependent backscattering of the retina, lens reflections, and both ophthalmic and optical system aberrations. Regardless of the design, any static optical system would have difficulties imaging a large FOV in the retina, as the magnitudes of ophthalmic aberrations vary both between patients and within patients according to eccentricity [13, 14]. Additionally, studies of the isoplanatism at the foveal region revealed isoplantic patches between 0.8° and 2.5° [15, 16], with individual variations as large as 6° [17]. Since multiple AO corrections would be required for a large FOV image, WF-OCT design may necessitate the incorporation of adaptive optics (AO) components.

Traditionally, AO wavefront correction has used closed-loop feedback in which a wavefront sensor detects and a deformable mirror (DM) compensates ocular aberrations [18–23]. Closed-loop configurations have been very successful in imaging foveal photoreceptors [24, 25], but wavefront sensors can restrict the design of imaging systems. For example, many AO imaging systems use off-axis mirror telescopes to avoid lens surface reflections [26] that interfere with wavefront detection. Often the off-axis mirror telescopes make use of long focal length and toroidal mirrors [27] in order to reduce static system aberrations [21, 28]. While not prohibitive to foveal imaging, these design choices offer trade-offs that could help expand closed-loop AO to new applications.

Recently, wavefront sensorless adaptive optics (WSAO) was applied to ophthalmic imaging applications, proving capable of acquiring high-resolution images in both rodent [29] and human [30, 31] eyes. WSAO eliminates the wavefront sensor-based feedback loop by iteratively correcting the wavefront shape through maximization of imaging metrics, such as brightness [32]. While WSAO mitigates problems due to improper wavefront detection, it corrects the wavefront shape more slowly. Higher-order correction was demonstrated over the

Biomedical Optics EXPRESS

course of tens of seconds [31] and low-order correction has been performed in as little as 6-12 seconds [30] during *in vivo* imaging of the human retina. In turn, WSAO offers versatility, in that it does not require a wavefront sensor, at the expense of wavefront correction speed.

In this work, we present an WF-OCT system equipped with wavefront sensorless adaptive optics (WSAO) that is capable of acquiring aberration-corrected images throughout a >70° visual field. Our proposed system acquires non wavefront-corrected wide-field OCT images without mosaicking, which are then used to locate smaller regions of interest that can be re-imaged with the benefits of WSAO. Our algorithm derives its speed from utilizing raw, unprocessed B-scan data (spectral interferograms) for computation of the optimization metric. The combination of a lens-based sample arm and WSAO may be well suited for clinical adoption, and we exhibit the utility of this new tool by imaging patients in a clinical setting. In particular, we used this system to enhance the visualization of anatomical and pathological features in the peripheral retina for neurologic diseases. To our knowledge, this represents the first example of imaging neurological diseases with adaptive optics OCT in the peripheral retina.

2. Methods

2.1. OCT sample arm and engine details

We designed a swept-source OCT imaging system with a custom wide-field sample arm (Fig. 1). We used a commercially available swept-frequency laser (Axsun Technologies, Inc.; MA) with a bandwidth of 100 nm, center wavelength of 1043 nm, and 100 kHz sweep rate. We coupled the output of the laser to a fiber-based Mach-Zender interferometer with polarization control and an initial splitting ratio of 80:20. The greater split of the power illuminated a retroreflector-based reference arm, while the lesser power illuminated the wide-field sample arm. The footprint of the sample arm was approximately 400 mm by 600 mm and was mounted on a slit-lamp base. The slit-lamp base provided a chin rest that aided in the stabilization and alignment of patients as well as the ability to translate the sample arm in the x, y, and z directions.

We modeled the optical design of the sample arm in ray-tracing software (Zemax, LLC; WA) using a wide-field optical model of the human eye [13]. According to Zemax ray-tracing simulations, the working distance from the apex of the final lens of the sample arm to the apex of the cornea was predicted to be 18 mm over an angular range of 70°, which approximated a 19.28 mm arc length on the retina of the model eye [13]. The angular extent of the sample arm was determined by simulating the largest angle in the ocular pupil plane of the chief ray with no vignetting of a 3 mm beam and using a 6 mm pupil diameter. The on-axis system performance ranged from a diffraction limited spot of 7.54 µm at the center wavelength (1043 nm) up to 10.5 µm at one edge of the spectrum (993 nm), corresponding to a beam size of ~3 mm. At the extreme of the off-axis angles, our simulations predicted a spot size of 45 µm on the retina of our model eye. This large number was expected due to off-axis aberrations in both the system and ophthalmic optics prior to wavefront correction.

From the 20% interferometer split, a small, achromatic parabolic mirror reflector (RC04APC-P01, Thorlabs, Inc.; NJ) collimated light into the sample arm. A relay telescope conjugated two 10 mm clear aperture galvonometers (GVS112, Thorlabs, Inc.; NJ). We separated the galvanometers in order to reduce the amount of wander in the ocular pupil plane, which increases with steeper angles of illumination. Additionally, the deformable mirror relay and the objective relay (Fig. 1) conjugated the galvanometers with the deformable mirror (Mirao-52e, Imagine Optic, Inc.; MA) and the pupil of the subject's eye. We mounted the entire sample arm on a modified adjustable slit-lamp base. We used a small computer monitor (Lilliput 869GL, Lilliput Electronics, Inc.; CA) that displayed a black background and red cross as a fixation target for the eye not being imaged.

The output signal of the WF-OCT system was detected by a 1.0 GHz InGaAs fiber-coupled balanced receiver (PDB481C-AC, Thorlabs, Inc.; NJ) and relayed to a high-speed

Biomedical Optics EXPRESS

12-bit digitizer (ATS9360, Alazar Technologies, Inc.; Quebec, Canada) that was triggered by the laser's optical clock port. The electrical output from the balanced receiver was attenuated using two RF attenuators (VAT-7 + , VAT-10 + , Mini-Circuits, Inc.; NY) and low-pass filtered (SLP-200 + , Mini-Circuits, Inc.; NY). In order to mitigate the residual effects of dispersion mismatch between the sample and reference arms, we applied numerical dispersion compensation during the image acquisition [33]. We acquired images with a custom GPU-accelerated C++/CUDA software program that utilized a high performance GPU (GeForce GTX Titan, NVIDIA Corporation; CA). The software program processed and displayed OCT images in real-time. The software was capable of processing 1.396 million A-scans/second with 1376 samples per A-scan, though the OCT acquisition was considerably below this limit.

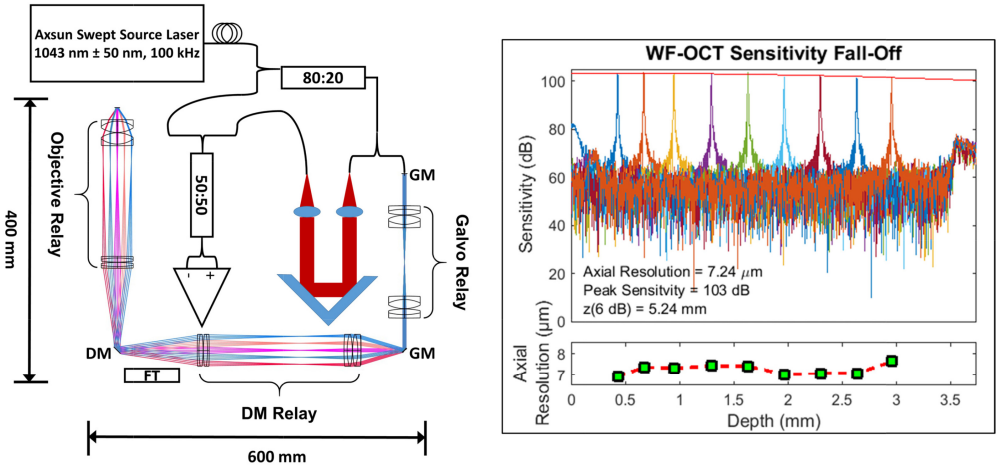

Fig. 1. System overview. A ray-tracing diagram of the wide-field sample arm shows the positions of the galvo mirrors (GM), galvo relay, deformable mirror (DM), fixation target (FT), deformable mirror relay, and the objective relay. The fall-off plot shows an axial resolution of 7.24 µm, a peak sensitivity of 103 dB, and a –6 dB fall-off of 5.24 mm. The red envelope is a double Gaussian fit to the peak of each pathlength difference.

We measured peak sensitivity and sensitivity fall-off plots for the WF-OCT system using a model eye. The model eye consisted of a 25 mm focal length lens (LB1761-C, Thorlabs, Inc.; NJ), a 45 dB double-pass neutral density filter (NENIR20A-C, NENIR20A-C, Thorlabs, Inc.; NJ), and a silver-coated mirror with tip, tilt, and axial-translation capabilities. The model eye had a similar pathlength to that of the adult human eye. We recorded A-scans at various pathlength differences between the model eye and reference arm. All of the A-scan peaks were recorded on-axis and with a flat DM shape. We generated a sensitivity fall-off envelope by fitting each A-scan peak to a Gaussian and then fitting a double Gaussian to the peak sensitivity measured at each pathlength difference (Fig. 1).

Characterization of the wide-field sample arm and OCT engine can be seen in the fall-off plot in Fig. 1. We measured a peak sensitivity of 103 dB with an axial resolution of 7.24 µm and a –6 dB sensitivity fall-off at 5.24 mm. The sample arm was capable of achieving a FOV of 70°, and we quantified the transmission of our sample arm to be 68%.

2.2. Wavefront sensorless adaptive optics operation procedure

We estimated and corrected wavefront aberrations by maximizing the sum of the absolute value of spectral interferograms of unprocessed B-scan data. Stationary B-scans at the same location were used while correcting the wavefront shape. The width of the B-scans varied from 1 to 7 mm (~3.5°-24.3°) according to the size of the volume that was to be imaged after WSAO optimization. WSAO correction was only applied to small volume patches; no correction was used on the wide-field 70° images as this FOV greatly exceeds the isoplanatic

Biomedical Optics EXPRESS

patch. A new wavefront correction was acquired immediately prior to each WSAO corrected image.

The WSAO optimization algorithm (Fig. 2) first swept through a series of 33 predefined defocus values (−8D to + 6D) and selected the defocus shape with the maximum intensity. The optimization then switched to a modified version of the stochastic parallel gradient decent algorithm [31, 35], wherein the perturbation size decreased as the B-scan intensity approached larger values. If at any point during the random perturbation sequence the B-scan intensity exceeded the brightest recorded intensity, the loop would break and update the current mirror shape with the brightest mirror shape (Fig. 2). The algorithm would then downscale the change in DM shape by a factor of 0.6 and continue applying the downscaled shape until no further improvement in brightness was found. We modified the method presented in [31] in order to achieve more repeatable performance on our static model eye (data not shown).

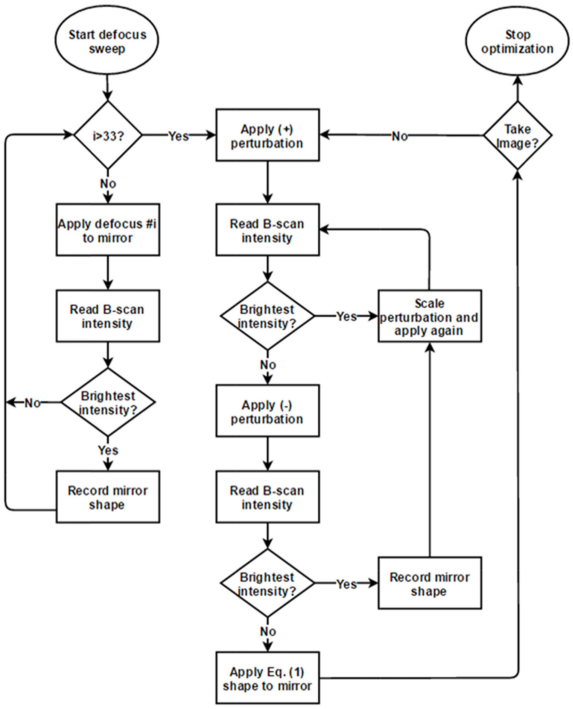

Fig. 2. Flow-diagram of the WSAO optimization algorithm. The first part of the algorithm (left path) swept through a range of predefined defocus values. After the coarse defocus was removed, the algorithm followed the stochastic parallel gradient descent technique laid out previously in [31]. If at any point the current brightness of the B-scan image exceeded the previously established maximum value, the algorithm broke and updated the mirror to the shape associated with the brightest image.

After initializing, the operator only needed to indicate when to stop the optimization procedure. A graph of the optimization metric was displayed in real-time for the operator. As the wavefront became corrected, the optimization metric would reach a maximum value. The operator then switched the system from correcting the wavefront to imaging the subject. For reference, the variation of the intensity metric when no optimization was occurring was roughly an order of magnitude smaller than the improvement after wavefront correction.

We applied parallel processing toolkits (OpenMP [34]) to calculate the optimization metric (<2 ms). Our custom C++/CUDA software permitted a new mirror shape to be calculated and applied without affecting the OCT acquisition. The Mirao52e mirror has a ~5

Biomedical Optics EXPRESS

ms settling time, which was the bottleneck in the WSAO optimization loop. Toggling of the DM from corrected to flat mirror shapes took ~5 ms, so the effects of both voluntary and involuntary eye movements [36] were minimized in B-scan image pairs.

For 1024 A-scans/B-scan (10 ms), we updated the mirror shape before the start of each subsequent B-scan; however, we acquired a full B-scan after the mirror had reached a steady state in order to perform the intensity calculation on a stable image. Therefore, each WSAO iteration would take 20 ms, and the entire optimization would last between 3 and 10 seconds. To our knowledge, 20 ms is the fastest WSAO iteration speed to date. If eye motion occurred during the defocus sweep, the operator restarted the WSAO algorithm. The stochastic parallel gradient descent was less sensitive to motion, as long as fixation returned to the original position.

In order to demonstrate that the WSAO algorithm (Fig. 2) was able to correct both defocus and higher-order aberrations, we studied the optimization process on the same model eye as was used to obtain the sensitivity fall-off plots. For this experiment, we replaced the mirror and neutral density filters with a diffuse scattering target. We ran the algorithm in the periphery of the model eye, approximately 19.25° off-axis along a meridian 45° from the horizontal. Vignetting did not allow us to perform the experiment beyond this radius. The B-scan size used to calculate the intensity metric was 1 mm for this experiment. A one-diopter trial lens was added to the set-up after achieving the best flat mirror focus on-axis. We recorded 40 independent optimizations, reporting the value of the optimization metric for each new mirror shape during the first 15 seconds of acquisition (Fig. 3(A)). In 40 additional runs, we allowed the optimization metric to reach steady state (~300 seconds). We plotted the Zernike coefficients applied to the DM after WSAO optimization using the Noll indexing scheme for Z4-Z11 (excluding piston, tip, and tilt) for both the 15- and 300-second optimization times (Fig. 3(B)).

2.3. Performance evaluation of WSAO in the periphery of the living human eye

We quantified the enhancement offered by WSAO in the periphery of the human eye by imaging four regions of the peripheral retina in each of five healthy volunteers (n = 5). We evaluated the performance of WSAO directly in the living human retina as opposed to a mock model eye with static target because the peripheral aberrations of mock model eyes differ greatly from those of actual human eyes. Only five of the total seven healthy volunteers were used in this experiment as we did not have ample time with each volunteer to run every type of experiment. Prior to imaging the periphery, each volunteer's central refraction was corrected with contact lenses or by adjusting the axial position of the final lens. Repeated (512 lateral x 1376 axial) B-scans 1 mm in length were acquired in the peripheral retina (>23° from the fovea) at inferior, superior, temporal, and nasal locations. Pairs of repeated B-scans with and without WSAO correction were acquired <100 ms apart. A new WSAO correction was obtained for each B-scan pair. The repeated B-scans were DC subtracted, dispersion compensated, log transformed, and averaged 5x prior to analysis. A threshold that excluded <0.75% of the outlier pixel values was used to scale the images to an 8-bit display range. A total of 40 B-scan images (four locations by five subjects by two mirror shapes) were chosen from the larger data set of 314 images by selecting image pairs with the largest brightness difference between flat and corrected DM shapes.

A two-way repeated measures ANOVA with two within-subjects factors (retinal location and DM shape) was used to contrast the change in mean B-scan intensity with and without adaptive optics correction (40 images). Across the entire processed B-scan width, we calculated the mean intensity per pixel between the vitreous-nerve fiber layer boundary and the visible choroid. The percent change in B-scan intensity was determined by averaging the ratio of mean B-scan pixel intensity for on-off image pairs. A Fischer's protected least significant difference post-hoc test was used to compare differences in image brightness with the data split by location.

Biomedical Optics EXPRESS

Changes in OCT spatial frequency content with and without WSAO were quantified from the same data set (40 B-scan images) acquired in four locations from each of five healthy volunteers (n = 5). We calculated the log of the absolute value of the radially averaged Fourier spectrum for each processed B-scan, and we used the sum of the radially averaged Fourier spectrum for $\omega/2 > 0.4$ as a measure of high frequency content, where ω is the frequency on a 2π normalized Fourier spectrum. A two-way repeated measures ANOVA with two within-subjects factors (retinal location and DM shape) was used to compare the difference in high frequency content with and without adaptive optics correction. The percent change in resolution was determined by averaging the ratio of high frequency content for on-off image pairs. A Fischer's protected least significant difference post-hoc test was used to compare differences in high frequency content when the data was split by location.

2.4. Patient alignment and clinical imaging protocol

The WF-OCT system was aligned to human volunteers by translating the slit-lamp base and adjusting the location of the fixation target until a foveal B-scan was centered with respect to the imaging system. Once centered, we switched the software program to a continuous wide FOV retinal volume scan (no WSAO correction) that spanned the full angular range of the system (70°). Real-time volume images were rendered *en face* as an un-averaged SVP. The wide-field images were comprised of approximately 1024 A-scans/B-scans and 1024 B-scans/volume. The reported FOV for a particular wide-field SVP was calculated as 70° times the ratio of the horizontal SVP length to the full horizontal scan length including black space. We used wide-field B-scans from the foveal region of the volume image to avoid clipping in the axial dimension.

We used the live feed of the wide-field scan to locate smaller regions of interest, such as those regions containing high vasculature or abnormal tissue. After the instrument operator selected a region from the wide-field scan, the software program adjusted the scan pattern to image only the targeted region. The targeted regions would vary in size according to the area that the operator selected, but were in the range of 1-7 mm for the data presented in this manuscript. In the scenarios where the targeted subfields exceeded the size of the isoplanatic patch, WSAO would result in a suboptimal corrected wavefront that was a best fit over the FOV being visualized. Repeated B-scans from the center of the volume were used in the WSAO process. After a corrected wavefront shape was obtained, an OCT volume was immediately acquired. A new WSAO optimization was performed prior to each acquisition. We critically sampled the smaller regions, typically with 1024 A-scans/B-scan.

Pairs of B-scan images were recorded in close succession (<100 ms) in order to visualize approximately the same location qualitatively. After a corrected mirror shape was obtained with WSAO, we toggled the DM between flat and WSAO corrected mirror patterns in order to generate a B-scan pair. For equal comparison of intensity, B-scan image pairs were contrast matched with the same intensity threshold such that white and black in the images corresponded to the same intensity values.

We compared volume images by acquiring image pairs sequentially with a flat or corrected mirror shape or by toggling the mirror shape midway through a single volume scan. New wavefront correction was obtained prior to acquiring each wavefront corrected volume. Raw intensity projections, such as summed voxel projections (SVPs) and maximum intensity projections, were used to compare the brightness of image pairs. Additionally histogram matching [37] of image pairs was used in order to compare the visibility of *en face* features without bias to brightness.

We registered and segmented retinal layers in OCT volume data with our previously developed DOCTRAP software [38], allowing for specific retinal regions, such as one containing the choriocapillaris or deep capillary layer, to be visualized independently. In order to demonstrate improved imaging of high frequency features with and without WSAO correction, we calculated the log of the absolute value of the radially averaged Fourier

Biomedical Optics EXPRESS

Spectrum for specific retinal layers within volume image pairs. The entire B-scan width was used in the calculations. Additionally, we integrated the high frequency content of the radially averaged Fourier spectrum for $\omega/2 > 0.4$ in order to quantify the overall change in high frequency content.

2.5. Clinical imaging details

A pilot trial of WF-OCT imaging with WSAO was conducted in nine human subjects in a clinical setting. The subjects were either healthy (n = 7) or had mild cognitive impairment, also known as prodromal Alzheimer's disease (n = 2) [39]. The optical power at the pupil plane was ~1.8 mW, which is below the 8-hour ANSI maximum permissible exposure limit for a static beam. Dilation of the volunteer's pupils was accomplished by darkening the room. All human subject research was approved by the Duke University Medical Center Institutional Review Board.

3. Results

3.1. WSAO algorithm performance

The time course of the WSAO algorithm taken in the periphery of the model eye was plotted in Fig. 3(A) for the first 15 seconds of optimization. The inset in Fig. 3(A) depicts the algorithm's performance over 300 seconds of optimization. These time plots are longer than the optimization time used while correcting aberrations in the living human eye (3-10 seconds) in order to demonstrate the steady-state behavior of the stochastic algorithm. The error bars correspond to the standard deviation of the optimization metric over the 40 runs for a given time point. It can be seen that a large portion of the aberrations are removed during the defocus sweep, which lasts less than 0.7 seconds (black vertical dashes, Fig. 3(A)). Afterwards, higher-order aberrations begin to get corrected. The stochastic parallel gradient descent portion of the WSAO algorithm is random, and as expected, the standard deviation of the optimization metric grows with time. While the algorithm does not reach a steady state within 15 seconds, Fig. 3(B) shows that the resulting wavefront correction applied to the DM after 15 and 300 seconds were very similar. Zernike coefficients were calculated from mirror voltages through multiplication with a calibration matrix recorded by a wavefront sensor. The root-mean-square error between the 15- and 300-second acquisitions was 0.0089 μm.

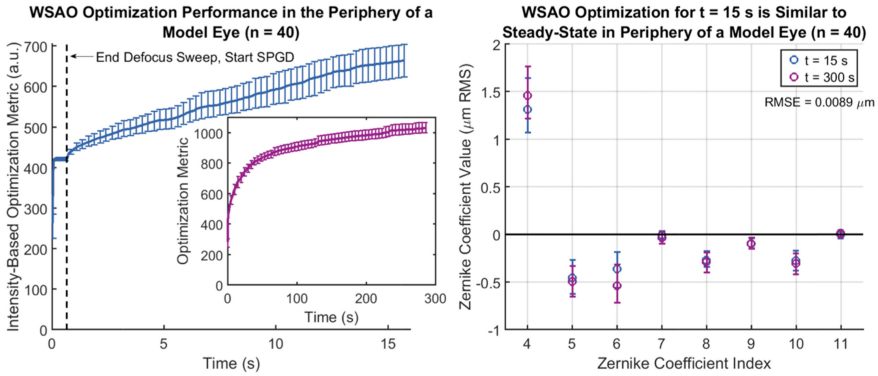

Fig. 3. Plots exhibiting the performance of the WSAO algorithm in the periphery (19.25° off-axis) of a static model eye. The time course over the first 15 seconds (left) and 300 seconds (left inset) demonstrated an increase in the optimization metric beyond the initial defocus sweep, suggesting that higher-order aberrations also were corrected. The error bars corresponded to the standard deviation over 40 WSAO optimizations. The corrected wavefront shape on the DM after 15 and 300 seconds was plotted (right), where the error bars once again corresponded to the standard deviation over 40 runs. The RMS error between the 15- and 300-second optimized DM shapes was 0.0089 μm. The high degree of overlap suggested that higher-order aberrations were being corrected reliably for the 15-second optimization window.

Biomedical Optics EXPRESS

3.2. Quantifying the increase in B-scan intensity and high spatial frequency content in the periphery of the living human eye

From the omnibus repeated measures ANOVA test for intensity, a main effect of WSAO correction was found with $p<0.05$, implying that WSAO correction resulted in a statistically significant increase in signal. Both location and the interaction of location with WSAO correction (slope in Fig. 4) were not statistically significant, suggesting that the magnitude of improvement offered by WSAO was not location-dependent. Post-hoc testing showed that at each location there was a significant increase in image brightness with WSAO correction. These results were visualized in Fig. 4 for both specific retinal locations and the combined total. An improvement in average pixel brightness of 10.4% and 5.9% was observed throughout the various locations for the 40 and 314 image data sets, respectively. It is important to keep in mind that the numerical values reported for the increase in average pixel brightness were calculated after the OCT images were $\log_{10}$ transformed. Additionally this metric averages intensity changes in retinal layers without much signal, such as the outer nuclear layer, in addition to those layers that are hyper-reflective, such as the photoreceptor layers and retinal pigment epithelium (RPE).

For the second omnibus repeated measures ANOVA test, performed on the radially averaged Fourier spectrum, a main effect of WSAO correction was found with $p<0.05$, which implied a statically supported improvement in high frequency content with WSAO correction. Once again, both location and the interaction of location with WSAO correction (slope in Fig. 4) were not statistically significant. Post-hoc testing showed that at each location there was a significant difference in high frequency content between WSAO on and off images. The mean B-scan resolution improvement with and without WSAO correction was plotted in the line graphs of Fig. 4. An average B-scan resolution improvement of 7.0% and 3.3% was observed throughout the various locations for the sets of 40 and 314 images, respectively. In 143 out of 157 image pairs (91%), an increase in mean B-scan intensity was accompanied by an increase in high frequency content.

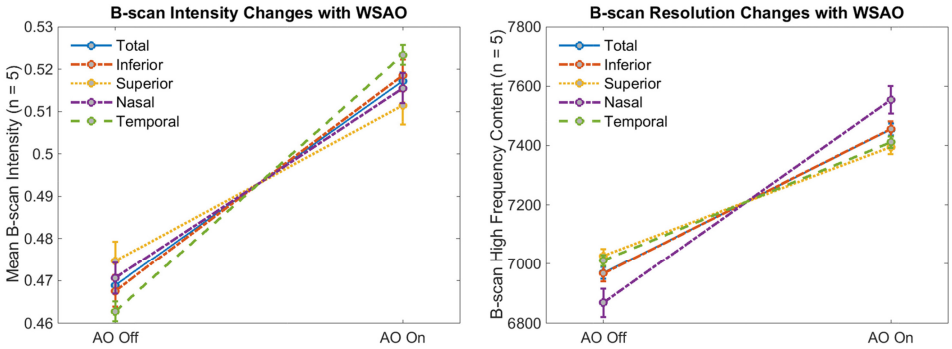

Fig. 4. Plots depicting the change in mean B-scan intensity (left) and high spatial frequency content (right) with and without WSAO correction at various locations in the peripheral retina (>23°). The error bars of the line plots correspond to the standard error (n = 5) for within-subjects variability. The lines connecting the pairs of points represent the interaction of the main effect of location with WSAO correction.

3.3. Imaging results of WF-OCT and WSAO in healthy eyes

Figure 5 exhibits the baseline imaging performance achieved by the proposed WF-OCT system without WSAO correction. Using WF-OCT, we acquired high-quality (1024 lateral x 1376 axial) foveal OCT B-scan images (Fig. 5(A)) that were comparable with smaller FOV imaging systems [40, 41]. Axially, the photoreceptor layers and external limiting membrane were visualized, while laterally, both the inner nuclear layer and choroid had defining

Biomedical Optics EXPRESS

features. With respect to image brightness, both the ganglion cell layer and inner plexiform layer were distinguished and the choroid was penetrated deeply.

The (1024 lateral x 977 lateral x 1376 axial) unaveraged wide-field SVP (Fig. 5(B)) taken with our proposed system was evidence that the FOV spanned the full angular range of the sample arm and was able to be acquired in a single continuous scan with minimal motion artifacts. The wide-field imaging mode was only used for locating regions of interest, so no WSAO was applied. Turning off the room lights helped dilate the volunteer's pupils and reduce vignetting. The ocular pupil was the limiting aperture of the optical system, as was evident in Fig. 5 where there was not a sharp boundary at the edge of the retina. WSAO correction can be applied to smaller subfields throughout the FOV spanned by Fig. 5(B) without changing subject fixation.

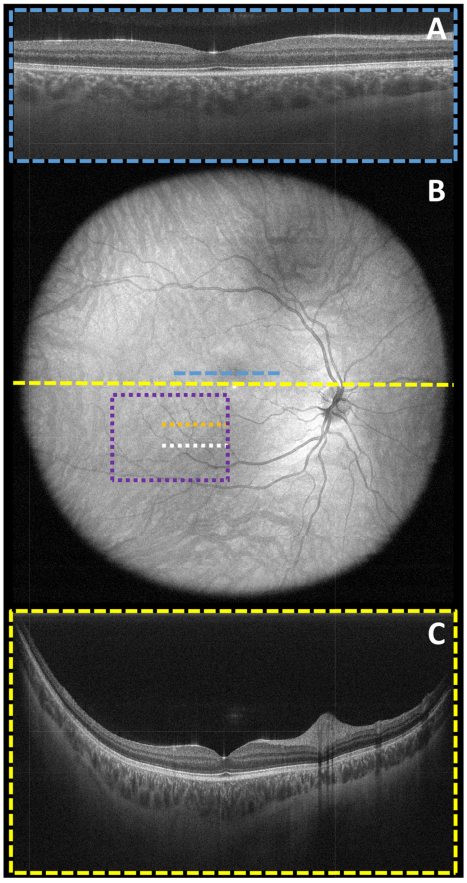

Fig. 5. Demonstration of WF-OCT system's large (70° or ~22 mm x 22 mm) FOV and uniform intensity distribution in a healthy volunteer. No WSAO correction was applied in these images. A 5x averaged foveal B-scan (A) with the deformable mirror in the flat position (AO off) was shown (blue dashed line) in context of the un-averaged wide field-of-view SVP (B), which depicted the imaging range of the wide-field sample arm. A 5x averaged wide-field B-scan (C) taken across the horizontal meridian (yellow dashed line) demonstrated good choroidal penetration even in the periphery of the retina. The orange and white dotted lines correspond to the locations of the independently acquired B-scan images shown in Figs. 6 and 8, while the purple dotted box corresponds to the independently acquired volume image of Fig. 7.

5x averaged (1024 lateral x 1376 axial) repeated B-scans (no WSAO correction) that spanned the central meridian of the volume scan (Fig. 5(C)) demonstrated strong tissue reflectance across the field-of-view. The various retinal tissue layers were distinguished both

Biomedical Optics EXPRESS

centrally and at relatively large eccentricities. In the far periphery, however, it was important to notice that the retinal layers began to blur together due to aberrations as the best focus was aligned to the foveal region. Additionally, deep choroid penetration allowed for defining features like blood vessels to be visualized, but with slightly less definition, in the peripheral extrema.

Peripheral (1024 lateral x 1376 axial) B-scans (Fig. 6), centered approximately 13° of radial eccentricity from the fovea, emphasized the qualitative differences in both brightness and resolution when using uncorrected (Fig. 6 left) versus WSAO optimized images (Fig. 6 right). These B-scans were centered on 13° eccentricity because there was not a similar region of dense vasculature located in the far periphery that could emphasize the enhancement in lateral resolution accompanied by WSAO optimization. Uncorrected images depicted the baseline peripheral image quality expected from our wide-field OCT system. The mean pixel intensity of Fig. 6 increased by 14.3% when the DM took the corrected wavefront shape. This increase in brightness was clearly distinguished in the RPE as well as the upper retinal cell layers. Blood vessels also exhibited an increase in brightness in their central regions as well as a sharper contrast in the shadowed layers below. The high frequency content of Fig. 6 improved by 7.4% with WSAO. An improvement in the sharpness of features was visualized in the region near the choriocapillaris as well as in the upper retinal vasculature. Bright vessel features (yellow arrows, Fig. 6) near the choriocapillaris appear clear in WSAO on images, whereas dull and blurry features were present in WSAO off images.

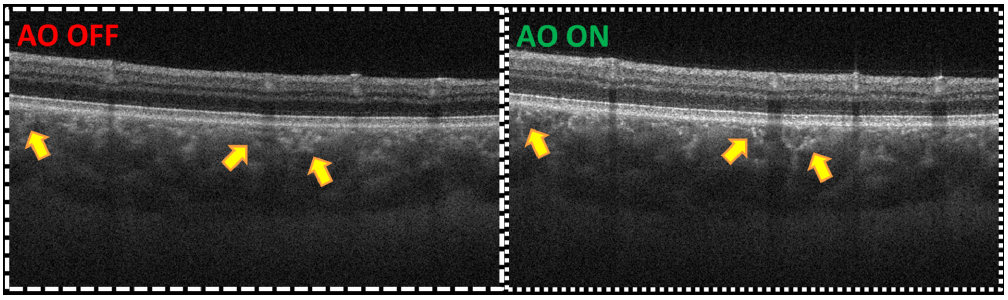

Fig. 6. Averaged (5x) repeated peripheral B-scan images (~3.4 mm wide) from the location marked by the white line in Fig. 5 when the deformable mirror had a flat (left) and optimized (right) mirror shape. The contrast levels were matched such that white and black corresponded to the same intensity value in the images. There was an increase of 14.3% in average pixel brightness and 7.4% in high frequency content with WSAO.

We contrasted the vasculature observed by two *en face* (815 lateral x 775 lateral x 1376 axial) maximum intensity projections (Fig. 7): one taken with a flat mirror shape (Fig. 7 top) and the other taken with a WSAO corrected mirror shape (Fig. 7 bottom). The two volumes were acquired at different time points (~10 s), but the ability to zoom into a region from the wide-field image made it relatively easy to navigate to the same imaging location. The images were centered at 15.5° of radial eccentricity and were ~6.0 mm wide. The edges of this FOV reached as far as 26°. The WSAO corrected image showed sharper and smaller vessel features, some of which were not observable in the flat mirror case (yellow arrows, Fig. 7). There was an obvious increase in image brightness of 9.6% after WSAO optimization as well. The digitally enlarged and histogram matched regions (Fig. 7 right) demonstrated that the clear differences in the visibility of vasculature were not a result of sub-optimally displayed images.

We extracted 5x spatially averaged (500 lateral x 1376 axial) B-scans (Fig. 8) from the volume data sets of Fig. 7 (orange dotted lines). Digitally enlarged regions surrounding blood vessels (colored boxes, Fig. 8) compared baseline peripheral OCT images (Fig. 8 top) with the same regions acquired with an aberration corrected DM shape (Fig. 8 bottom). WSAO optimized images were brighter than regular OCT B-scan images. The brightness increase

Biomedical Optics EXPRESS

with WSAO was especially localized to the inner plexiform layer, inner nuclear layer, and photoreceptor layers. The digitally enlarged images of Fig. 8 also highlighted the areas of the B-scan in which lateral resolution improvements from WSAO were most clearly visualized. There were much sharper retinal vessel boundaries and choroidal features (yellow arrows, Fig. 8) when WSAO was used. Overall, Fig. 8 asserted how WSAO optimization can improve the image brightness and clarity in the periphery of healthy human eyes.

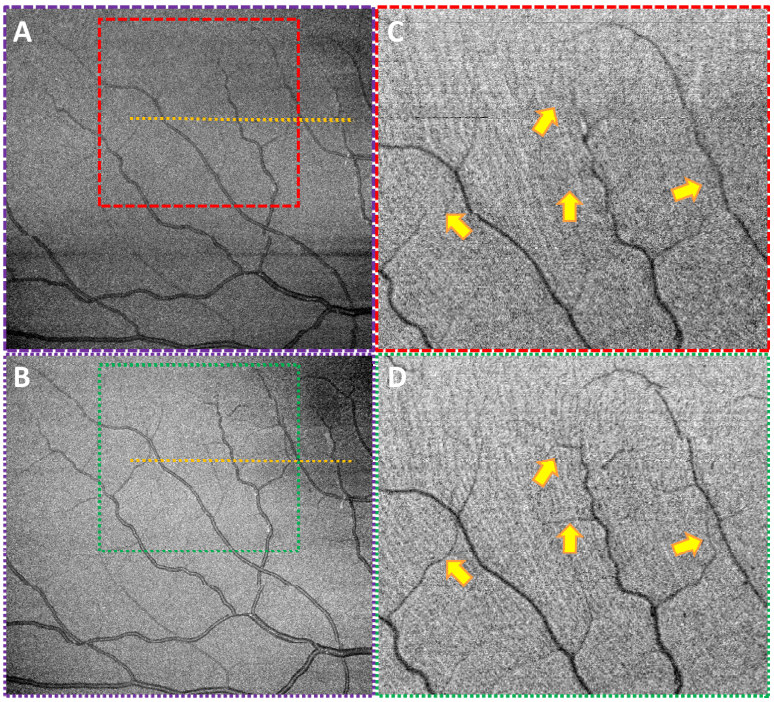

Fig. 7. Maximum intensity projections (A, B) of the region indicated by the purple box (~6.0 mm x 4.4 mm) in Fig. 5 when the deformable mirror conformed to the flat (top) and optimized (bottom) mirror shapes. The contrast levels were matched in the left pair of images such that white and black in the images corresponded to the same intensity values. The area bounded by the colored boxes in the left pair of images were enlarged digitally and histogram matched (C, D) in order to more fairly compare vessel visibility without bias to image brightness.

We exhibited the enhanced visibility of high frequency features due to WSAO optimization for various retinal tissue layers (Fig. 9). The (500 lateral x 500 lateral x 1376 axial) maximum intensity projected image (white dash-dot boxes) demonstrated the point in the volume scan where the mirror shape was toggled from a flat (bottom-half Fig. 9) to corrected (top-half Fig. 9) mirror shape. Tracing a single vessel across the toggle boundary, the vessel boundary got blurrier and enlarged due to the loss of lateral resolution.

SVPs (988 lateral x 988 lateral x 1376 axial) of two retinal layers (yellow and blue boxes, Fig. 9) were generated to contrast the visibility of features in specific layers with and without WSAO. While it could be observed qualitatively that there were smaller, brighter, and more sharply defined features in the region containing the choriocapillaris (yellow dotted boxes, Fig. 9), a radially summed Fourier spectrum showed an increase of 17.0% in the high frequency content when using WSAO. The region containing the choriocapillaris was defined as a 0.16 mm depth range below Bruch's membrane. The deep choroid layer, defined as 0.16-0.48 mm below Bruch's membrane (dashed blue boxes, Fig. 9), exhibited a similar, though slightly less obvious, 10.4% increase in high frequency content, which was to be expected as the deep choroid had larger, low frequency features. Also, there was a distinct increase in image brightness of 15.6% between the two regions of Fig. 9.

Biomedical Optics EXPRESS

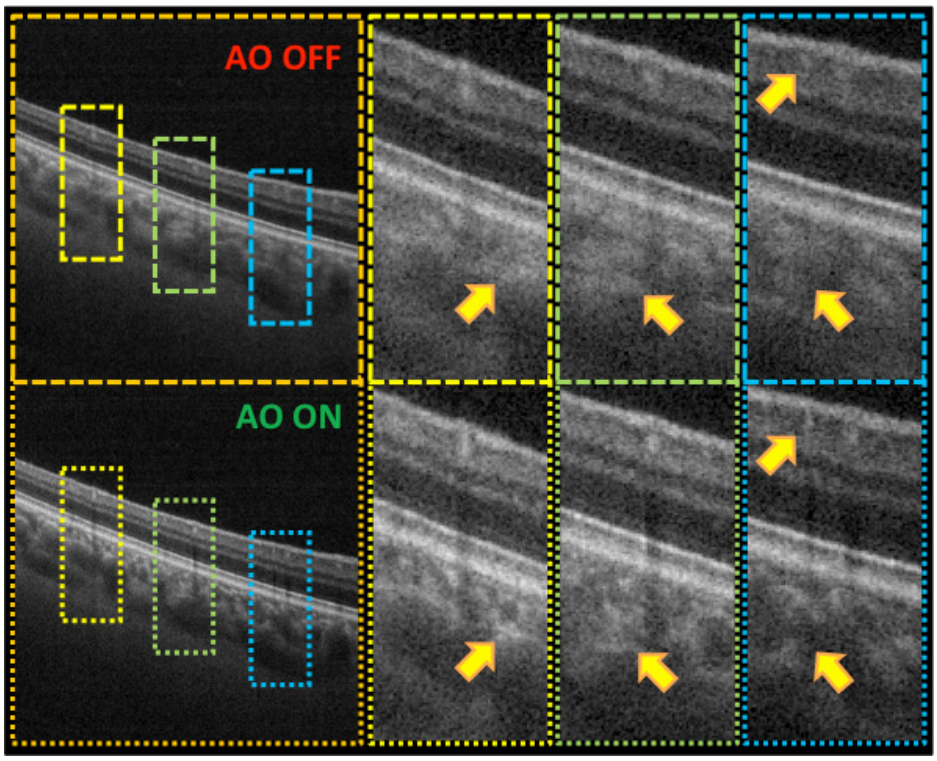

Fig. 8. Spatially averaged (5x) peripheral B-scan images (~3.4 mm wide) taken from the location marked by the orange line in Figs. 5 and 7 when the deformable mirror had a flat (top) and optimized (bottom) mirror shape. The image pairs were contrast matched. The small colored boxes are digitally zoomed regions from the large image on the left.

3.4. Imaging results of WF-OCT and WSAO in eyes with pathology

The data of Fig. 10 was acquired in a volunteer Alzheimer's suspect with mild cognitive impairment and 2 + nuclear sclerosis cataracts. In the centrally located (1024 lateral x 1376 axial) wide-field B-scan (dotted yellow line, Fig. 10 bottom), the region near the fovea looked healthy; however, at the left extent of the periphery (>30°), some slight pathologies (yellow arrow, Fig. 10 bottom) emerged in the RPE layer. A 12.5° peripheral (725 lateral x 1376 axial) wide-field B-scan (dashed blue line, Fig. 10 top) exhibited pathologies that extend from the periphery to even more centrally located regions of the eye.

After identifying a general region of pathology in the 65° wide-field SVP (no WSAO correction), we zoomed into an area of interest (purple dotted box, Fig. 10) and imaged it with the benefits of WSAO. The (725 lateral x 400 lateral x 1376 axial) volume and (725 lateral x 1376 axial) B-scan data of Fig. 11 were single, un-averaged images where the contrast levels were matched such that white and black corresponded to the same intensity values.

We show in Fig. 11 the effect of using WSAO when acquiring high-resolution images in eyes with neurodegenerative diseases such as Alzheimer's disease. In Fig. 11, WSAO increased the brightness of ~27° peripheral maximum intensity projected volumes (925 lateral x 200 lateral x 1376 axial) by 26.3% and made fine features sharper: the inner nuclear layer was better separated from the plexiform layers, and the choroidal vasculature was more clearly defined. While the brightness of the bulges in the photoreceptor layer looked relatively uniform in the flat mirror case, a clear change in brightness across the B-scan (925 lateral x 1376 axial) was observed in the outer photoreceptor layer when imaged with the corrected mirror shape. In the left portion of the B-scan images of Fig. 11, the retinal layers could not be distinguished, and therefore segmented, without WSAO.

Biomedical Optics EXPRESS

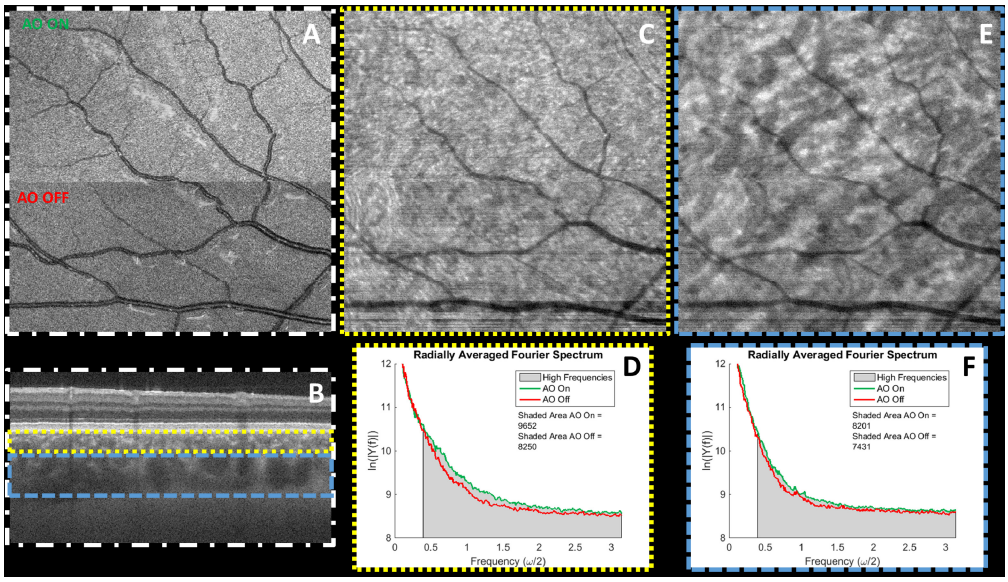

Fig. 9. Panel showing the differences in structure in a maximum projection image (~5.0 mm x 5.0 mm) of the retina (A, white dashes and dots), SVP of the region containing the choriocapillaris layer (C, yellow dots), and SVP of the deep choroid layer (D, blue dashes) when the deformable mirror was turned from off (bottom half) to on (top half) midway through the scan. The B-scan image (B) shows the location of the retinal layers used to display the SVPs of the various retinal layers. Radially averaged Fourier Spectrum (E, F) were plotted for the AO off (red line) and on (green line) portions of the SVPs. An increase in high frequency content was seen visually from the SVPs and quantitatively from the graphs of the radially averaged Fourier Spectra.

4. Discussion

4.1. Isoplanatic patch over a wide visual field

Aberration correction retains the highest fidelity within the isoplanatic patch [42]. Since the aberrations of the human eye vary with retinal eccentricity, it was important to consider the region of isoplanatism when designing the WSAO subcomponent of our system. Using the wide-field eye model of [13], we plotted the RMS wavefront error versus retinal eccentricity (Fig. 12). The eye model of [13] was generated from measured wavefront aberration data acquired in a population of 101 eyes [14] and represents the mean of the population. The eye model was designed with a 4 mm pupil diameter in order to match the pupil size of the measured population.

Figure 12 demonstrates that wavefront error is dominated by defocus and astigmatism in the peripheral regions. Figure 12 also shows that the magnitude of wavefront error varies more rapidly in the periphery. Following the work of [43], isoplanatism is defined as field variations in RMS wavefront error less than $\lambda/2\pi$ = 0.17 μm (λ = 1043 nm). Given this definition, the quadratic shape of Fig. 12 indicates that the isoplanatic patch size varies in accordance with retinal eccentricity. In order to recover some of the isoplanatism lost to the rapidly varying aberrations of the peripheral retina, we opted to use a smaller beam diameter of 3 mm. In comparison to the 6-7 mm beams that are typically used in closed-loop adaptive optics, a 3 mm beam will emphasize correction of lower-order aberrations, such as defocus and astigmatism, and have a larger diffraction limited spot size. Since low-order terms dominate peripheral aberrations, correcting them can help in achieving a more uniform lateral resolution, albeit within one isoplanatic patch at a time.

Biomedical Optics EXPRESS

4.2. Design trade-offs using a 3 mm beam diameter

Availability of galvanometers with high scan speeds, wide angle ranges, and large clear apertures limited the sample arm design. In order to use uniform magnification optical relays, we needed galvanometers that supported a >3 mm beam at an optical scanning range of +/–40°. By geometry, this imposed a minimum clear aperture of beam diameter/cos(steering angle + mechanical scanning angle). A 3 mm beam diameter, 20° mechanical scanning angle, and 45° angle to steer the beam in a new direction, resulted in a clear aperture of 7 mm. It is important to note that the steering angle can be reduced only until the physical hardware components begin to overlap, which is equivalent to twice the mechanical scanning angle. In order to keep up with the 100 kHz A-line rate of our OCT engine, a >7 mm diameter galvanometer would need to scan its full angle range in 10 ms for 1000 A-scans per B-scan. We were unable to achieve these specifications with commercial galvanometers.

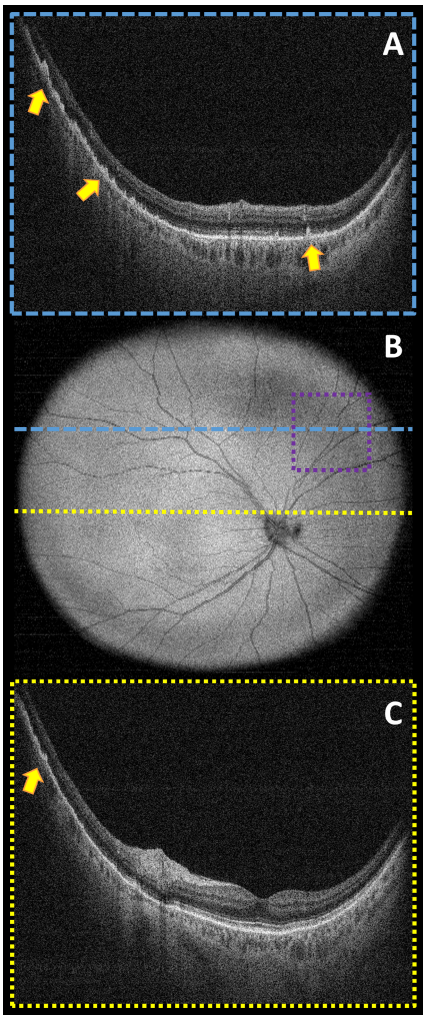

Fig. 10. Un-averaged wide-field (65° or ~20.5 mm x 20.5 mm) images taken from a subject with mild cognitive impairment (prodromal Alzheimer's disease) and cataracts. The colored lines in the wide-field image (B) corresponded to the peripheral (A) and central (C) B-scan locations. The peripheral B-scan image showed clear retinal pathology (yellow arrows) throughout the horizontal scan, whereas the central B-scan image only showed pathology in the extreme of the horizontal scan (yellow arrow). The purple dotted box represents the location of the volume image of Fig. 11.

Biomedical Optics EXPRESS

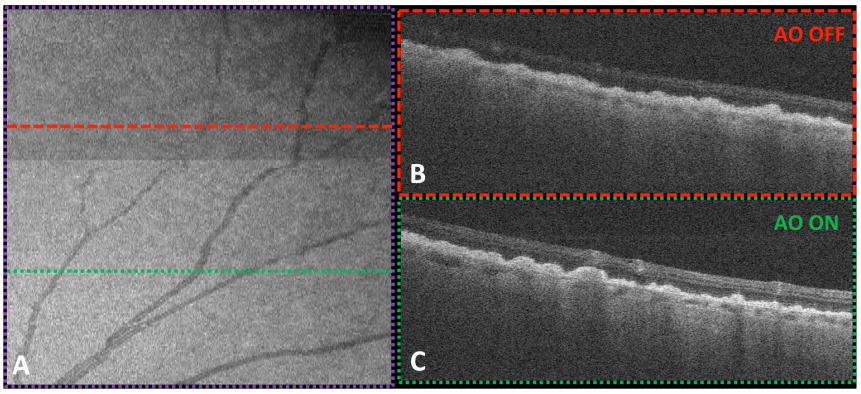

Fig. 11. Maximum intensity projection (A) of peripheral (27°) vasculature when the deformable mirror was switched between the unoptimized (top) and optimized (bottom) mirror shapes. WSAO increased the brightness of the *en face* volume projection (~4.4 mm x 4.4 mm) by 26.3%. Corresponding B-scans for regions without (B) and with (C) wavefront correction were shown on the right. The volume image was acquired in the location indicated by the purple dotted box in Fig. 10.

Alternatively, angle magnification after the galvanometer relay, as was used in our final design (Fig. 1), loosened the specification on the angle range and, subsequently, the minimum clear aperture diameter. Angle magnification, however, was coupled with beam diameter demagnification. In order to account for this loss, a larger beam diameter was used at the input to the system, but not so large as to exceed the galvanometer clear aperture. As we had a DM with a 15 mm pupil diameter and wanted to magnify the beam to fill its active area, magnifying relays were natural choices for our sample arm design. Additionally, since we anticipated defocus and astigmatism on the order of a few diopters in the periphery [13], we did not place the DM at the start of the imaging system because the wavefront corrected beam might clip at the galvanometers. Overall, the angle range and clear aperture for high scan speed galvanometers shaped the design of our WF-OCT sample arm.

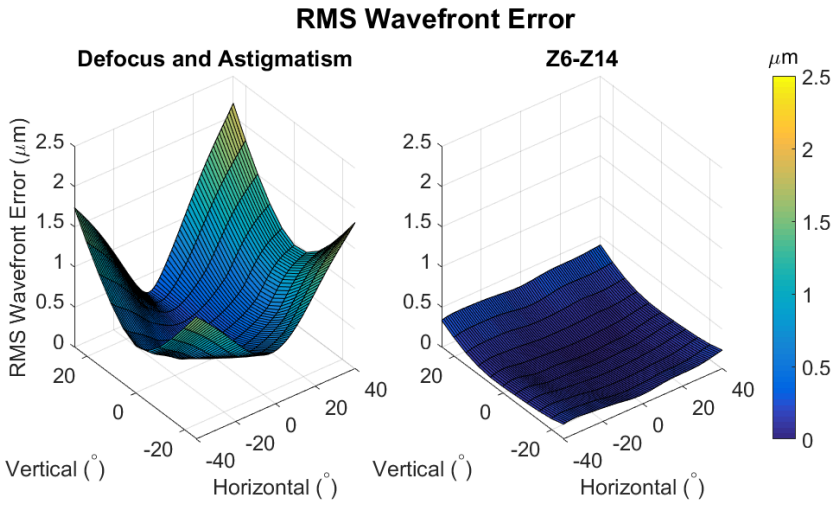

Fig. 12. RMS wavefront error versus retinal eccentricity as predicted by a wide-field eye model [13] for low-order (left) and high-order (right) aberrations. The eye model was designed to reproduce the mean aberrations measured in 101 eyes. A 4 mm pupil was used to generate this data. Both the magnitude and rate of change of RMS wavefront error are greatest in the periphery, where low-order aberrations dominate.

Biomedical Optics EXPRESS

We designed and built our sample arm using off-the-shelf commercial optics. While custom lenses may achieve smaller working distances, better angular support, precise angular magnification, and the ability to preemptively compensate angle-dependent ocular aberrations, low-dispersion wide-angle custom lenses can be very expensive. As the most influential aberrations in the retinal periphery are low-order (Fig. 12), correcting field curvature with a few custom lenses would permit a lower dynamic range DM to be used. However, while custom lenses may be able to correct the population average, individual variation in wavefront error could be as large as 0.5 µm [13]. With this in mind, we chose to use the extra dynamic range of the DM to remove the system aberrations in addition to the aberrations of the human eye.

In order to obtain the greatest benefit from adaptive optics, a large 6-7 mm diameter beam should enter the eye. Unfortunately, pupil wander is an especially difficult issue in WF-OCT as the beam begins to vignette substantially at larger eccentricities. We conjugated the two orthogonal galvanometers using a uniform magnification 4*f* relay in the current design. According to our Zemax simulations, this resulted in pupil wander of ~1.7 mm at 35° eccentricity. Given a 3 mm beam diameter, the beam should avoid clipping at the pupil and galvanometer scanners. While a slightly larger beam diameter could have been incorporated without vignetting, obtaining precise angle magnification would require custom lens relays.

In summary, we were able to achieve a +/–35° angle range for a 3 mm beam diameter using commercially available lenses and galvanometer scanners. Using Zemax ray-tracing simulations, we verified that vignetting should not occur throughout this angle range given a maximum pupil wander of ~1.7 mm and a 3 mm beam diameter. Given that the peripheral aberrations are strongly influenced by low-order terms, a 3 mm beam diameter was well suited to correct these aberrations at the expense of a larger diffraction limited spot size. Custom lens designs could have enabled more optimized solutions, although we selected less expensive commercial optics and used a DM with a large dynamic range to account for both system and patient aberrations. While the overall wavefront correction may have been suboptimal, our results demonstrated that WSAO correction with a 3 mm beam was sufficient to visualize features of interest in the peripheral retina, such as blood vessels (Fig. 7) and the drusen-like structures in Alzheimer's disease suspects (Fig. 11). Future studies may wish to explore the advantages of using larger beam diameters, but in this study, hardware was not available that permitted a larger beam diameter.

4.3. Trade-offs of WSAO versus closed-loop AO

The main reason we chose WSAO over traditional closed-loop AO is due to WSAO's versatility in the design of the WF-OCT sample arm. WSAO permitted us to design a smaller sample arm footprint since we did not have to include a wavefront sensor. In comparison, closed-loop adaptive optics systems use long focal length toroidal mirrors [27] to reduce optical aberrations and to prevent surface reflections from interfering with the wavefront sensor measurement [26]. In order to obtain a large (>70°) field-of-view, reflective telescopes would need to be used in very off-axis arrangements to avoid beam clipping. The steep angles of incidence would likely result in large magnitudes of off-axis aberrations, such as astigmatism and coma.

Lens-based closed-loop AO systems minimize surface reflections through polarization [26] or coherence [44] gating, although it is important to keep in mind that these systems are still vulnerable to improper wavefront detection. Closed-loop AO aberration correction is only as good as the wavefront detection accuracy [45], and weak wavefront signals are particularly relevant to this study because many of our target population have cataracts. Additionally, off-axis wavefront detection, as was the case for our WF-OCT system, is prone to error and requires the use of sensitive phase unwrapping techniques [46]. If a reliable wavefront measurement cannot be achieved, closed-loop correction is not possible. Eliminating the wavefront sensor afforded flexibility in the design of our lens-based wide-

Biomedical Optics EXPRESS

field sample arm, and future iterations may seek to incorporate a wavefront sensor in order to be able to account for faster aberration dynamics.

WSAO is less sensitive to eye motion because it integrates wavefront correction over the course of 3-10 seconds. As long as the majority of WSAO correction occurs within an isoplanatic patch, the effects of eye motion are mitigated. Unfortunately, this also means that WSAO is unable to correct for temporal dynamics in the ocular aberrations. This subsequently implies that WSAO may not be able to provide as good of wavefront correction as closed-loop AO, unless its convergence time is improved. If the convergence time of WSAO was similar to closed-loop AO, then WSAO would suffer from similar issues related to eye motion. Overall, optimization time plays an important role when correcting wavefronts *in vivo* due to the parasitic effects of voluntary and involuntary patient motion [36] as well as tear film dynamics [47, 48]. Despite the aforementioned shortcomings, our initial clinical encounters showed that WSAO provided sufficient aberration correction for enhanced visualization of important peripheral features.

4.4. Trade-offs of a WSAO intensity metric calculated from unprocessed B-scan data

Because we calculated our intensity metric from unprocessed B-scan data rather than processed volume data, our WSAO iteration speed was considerably faster than previous WSAO-OCT techniques [29, 30, 32, 49]. For example, the acquisition time required to obtain even a relatively small volume (300 lateral x 100 lateral x 1376 axial) is on the order of 300 ms for a 100 kHz A-scan rate. At the same A-scan rate, our 1024 A-scans/B-scan data can be acquired in 10 ms, so we can iterate our mirror up to 30x faster than volume-based iteration methods. Since WSAO algorithms take 100-1000 iterations to correct the wavefront shape [32, 50], iteration speed becomes proportional to the total optimization time. Improving the convergence speed [50] or robustness to eye motion of the optimization algorithm is another topic of interest, although it is outside the scope of this manuscript. To our knowledge, this was the first report of a WSAO optimization metric using raw spectral interferograms.

Using an intensity metric calculated from unprocessed B-scan data had trade-offs. Previous works used the summed intensity of processed OCT images as their optimization metric. By Parseval's theorem, power is conserved through a Fourier transform. Therefore, summing the intensity in the spatial domain was mathematically equivalent to summing the intensity in the spectral domain. Taking advantage of this relationship allowed us to eliminate the Fourier transform and iterate our WSAO technique at higher speeds. The downside of this technique was that we were unable to select specific retinal layers or focal planes. Rather, our technique resulted in a wavefront that maximized the collective signal from all retinal layers. As the retinal nerve fiber layer and photoreceptors contributed the largest signal intensity, our WSAO technique applied greater weight to the correction of these two layers but still had an impactful effect on other regions such as the one near the choriocapillaris (Fig. 9). While calculating the optimization metric from specific retinal layers may be possible, this approach may be more complex and computationally expensive to perform in the spectral domain.

4.5. Applications for aberration correction in WF-OCT

Increasing the signal intensity with WSAO leads to better defined retinal layers in the peripheral region of the eye. Visibility of retinal layers is important when diagnosing ocular diseases [51] as well as when monitoring a patient's responsiveness to treatment [52, 53]. Retinal layer thickness is an important biomarker of ocular diseases including glaucoma [51], retinitis pigmentosa [54], diabetic macular edema [55], and age-related macular degeneration [52, 53]. For example, a thinning retinal nerve fiber layer can indicate a loss of ganglion cells, which can lead to peripheral and then central vision loss [56]. Additionally, categorizing the source of retinal thickness changes into geographic atrophy [57] and drusen [53] can help when evaluating the severity of age-related macular degeneration [52]. Increasing signal with adaptive optics may improve the accuracy of segmentation when measuring layer thicknesses

Biomedical Optics EXPRESS

[38] or closed-contoured features [58] such as photoreceptors or blood vessels. By increasing the OCT signal in the peripheral retinal, the additional layer-specific details afforded by WSAO may enable manual and automatic segmentation algorithms to study the evolution of disease processes that would otherwise not be accessible.

Improving the lateral imaging resolution with WSAO also can be important for clinical imaging systems. We justified an increase in imaging resolution with WSAO by measuring a statistically significant increase in high frequency content in the B-scan image pairs of Fig. 4 and the *en face* projected images of Fig. 9. This approach is analogous to prior AO studies where cone spacing and other high frequency features are compared using Fourier spectra [22, 59].

We anticipate that the improved high frequency content offered by WSAO will be of particular interest when imaging intricate microvascular networks. We hypothesize that WSAO can better visualize the site of a retinal blockage or microaneurysm when assessing and treating diabetic retinopathies [5, 8]. Additionally, wide-field OCT angiography [60, 61] may offer a promising alternative to fluorescein angiography [9, 62], which can aid in the evaluation of diabetic macular edema. Many disease biomarkers manifest in the peripheral retina [5, 8, 9, 62], and earlier visualization of these diseases could lead to more effective treatment strategies.

WF-OCT with WSAO capabilities may provide key insights when observing the various stages of a given pathology. For example, it was interesting to visualize the distribution of drusen-like structures under the RPE layer of the prodromal Alzheimer's subject in Fig. 10. These structures appeared in the periphery, but not in the central macula. We note that the drusenoid structures in dry age-related macular degeneration tend to be more frequent in the macula [52]. Thus, a larger study is warranted to investigate the origins and pathologic significance of these potential imaging biomarkers of early Alzheimer's disease.

In current wide-field OCT systems, the peripheral regions of the eye are dim and difficult to observe [12]. While averaging can help to recover signal intensity, it would also increase motion blurring and subsequently reduce the system resolution. Additionally, averaging cannot improve the lateral resolution by correcting optical aberrations. In comparison to WSAO, averaging not only results in an inferior image, but obtaining a sufficient number of redundant images is not always possible in a clinical setting.

4.6. Advantages of wide-field imaging

Our custom wide FOV OCT sample arm enabled our system to switch rapidly between wide-field SVPs (Figs. 5, 10) and targeted regions of interest (Fig. 11), and to image the same area of interest multiple times (Fig. 7). Switching from a wide-field scan to a targeted high-resolution scan was seamless from the viewpoint of the volunteer, as they needed only to maintain fixation. Volunteers did not have to adjust their gaze nor did the system need to be realigned in order to image different regions of the retina.

Figure 10 illustrated the utility of the wide-field scanning mode in locating peripheral pathologies. With limited field-of-view commercial OCT systems or two-dimensional *en face* imaging systems, most of the pathology in this subject would have been difficult to observe. Even the central portions of the B-scan of Fig. 10 top are not typically accessible with commercial systems. With WF-OCT, the location of peripheral pathologies potentially could be identified in un-averaged wide-field SVPs.

4.7. Effect of retinal curvature on WF-OCT

The curvature observed in Figs. 5 and 10 were due to the pathlength mismatches between the peripheral retina and the reference arm. It is important to keep in mind that this curvature was not a direct measurement of the eye's physical shape [63]. The curvature at the periphery of the retina could be exaggerated by adjusting the pupil entry position of the beam. If the beam did not enter near the center of the pupil, the retina would appear exceptionally curved [64]

Biomedical Optics EXPRESS

and sometimes extend beyond the depth range of our system. We incorporated extended depth imaging [65] into our WF-OCT system, which was able to account for this additional curvature, though it was not always necessary if good patient alignment was achieved.

5. Conclusion

In this paper, we demonstrated a novel WF-OCT system equipped with WSAO for enhanced imaging of targeted subregions of the retinal periphery. Our relatively compact (400 mm x 600 mm) lens-based WF-OCT sample arm achieved a 70° field-of-view, which is twice the FOV of many commercial OCT systems, and allowed us to locate pathologies rapidly in a wide field-of-view scan, zoom into pathological features, find the same targeted region at different time points, and search around a targeted area of interest. Since fast DM iteration speed was important, we developed a WSAO technique that could iterate at the speed of individual B-scans (~20 ms) by computing the optimization metric from raw spectral interferograms. With WSAO wavefront correction, we quantified in the living human peripheral retina a 10.4% increase in B-scan intensity and a 7.0% increase in the radially averaged Fourier spectrum for high frequency features. Specifically for the region containing the choriocapillaris and deep choroid layers, we observed a 17.0% and 10.4% increase in high frequency content with WSAO. A pilot clinical study on seven healthy volunteers and two subjects with prodromal Alzheimer's disease showed the enhanced visualization of anatomic and pathologic features in the peripheral retina with WSAO wavefront correction. Overall, WSAO helped to distinguish tissue layer boundaries, fine details of the choroid, and smaller microvasculature. WF-OCT could even identify the location of pathologies as far as 32.5° from the fovea in raw un-averaged B-scans. Further optimization of the WSAO technique could aid in WF-OCT's widespread adoption in the diagnosis and treatment of ocular, and potentially neurodegenerative, diseases of the peripheral retina, including diabetes and Alzheimer's disease.

Funding

National Eye Institute of the National Institutes of Health (R01EY022691); North Carolina Biotechnology Center (NCBC) (IDG 2012-1015); Duke Institute for Brain Sciences (Research Incubator Award); National Science Foundation Graduate Research Fellowship to James Polans (DGE-11-06401).

Acknowledgments

We are thankful for the help and support provided by Dr. Anthony Kuo in the imaging of normal and clinical volunteers.